applied sciences

MDPI

Article

Dynamic Energy Efficient Control of Induction Machines Using Anticipative Flux Templates

Antony Dominic †,‡, Gernot Schullerus †,‡ and Martin Winter *,†,‡

Reutlingen Energy Centre, Reutlingen University, 72762 Reutlingen, Germany; Antony.Dominic@Reutlingen-University.de (A.D.); Gernot.Schullerus@Reutlingen-University.de (G.S.)

* Correspondence: Martin.Winter@Reutlingen-University.de; Tel.: +49-7121-271-7013

† Current address: Reutlingen University, Alteburgstr. 150, 72762 Reutlingen, Germany.

‡ These authors contributed equally to this work.

Abstract: Energy efficiency optimization techniques for steady state operation of induction machines are the state-of-the-art, and many methods have already been developed. However, many real-world industrial and electric vehicle applications cannot be considered to be in steady state operation. The focus of this contribution is on the efficiency optimization of induction machines in dynamic operation. Online dynamic operation is challenging due to the computational complexity and the required low sample times in an inverter. An offline optimization is therefore conducted to gain knowledge. Based on this offline optimal solution, a simple and easy to implement template based solution is developed. This approach aims at replicating the solution found by the offline optimization by resembling the shape and anticipative characteristics of the optimal flux trajectory. The energy efficiency improvement of the template based solution is verified by simulations and measurements on a test bench and using a real-world drive cycle scenario. For comparison, a model predictive numerical online optimization is investigated too.

Keywords: energy efficiency; induction machines; optimization; dynamic operation; loss minimization

Citation: Dominic, A.; Schullerus, G.; Winter, M. Dynamic Energy Efficient Control of Induction Machines Using Anticipative Flux Templates. *Appl. Sci.* **2021**, *11*, 2878. https://doi.org/10.3390/app11062878

Academic Editors: Tomonobu Senjyu and Claudio Bianchini

Received: 29 January 2021
Accepted: 17 March 2021
Published: 23 March 2021

1. Introduction

Electric drives have always been a key component of any automated process. The ongoing drive to automate every single aspect of a production process combined with the added intelligence of the Fourth Industrial Revolution have induced a renewed research interest in electric drives. In parallel, we are witnessing the widespread adoption of electric vehicles, in particular cars, trucks, automated logistics vehicles, and electric bikes. Whenever mentioning electric mobility, it is necessary to evaluate the technological and sociological boundaries. The restricted capacities of energy storage technologies are a limiting factor. The concerns about negative environmental impacts throughout the production process, lifetime, and dismantling process of a product must be addressed. For these reasons, an electrically propelled future must use energy, cost, and resource efficient drive systems.

Highly energy efficient electric machines are typically obtained by using permanent magnet or separately excited synchronous machines. However, permanent magnets cause a variety of issues [1]. From an environmental point of view, the extraction of the needed rare earth materials is a polluting process, and these materials can yet not be recycled after the motors' lifetime. The global market for rare earth materials is nearly a single source situation, which is not desirable for any manufacturer, as they are furthermore confronted with high prices and high price fluctuations. The manufacturing process of both permanent magnet and separately excited synchronous machines is complex, which also results in higher overall costs for this machine type.

Induction machines are used in industrial applications and electric mobility due to their very simple design and operation compared to other machine types. This simplicity leads to a more cost and resource efficient manufacturing process. No permanent magnets

are required, which eliminates most of the negative aspects mentioned above. This is the case for synchronous reluctance machines as well. An energy efficiency comparison was given in [2], and an easy optimization method based on minimal power per torque was given in [3]. In addition, there are particular measures required in the field weakening operation of induction machines compared to permanent magnet synchronous machines. Induction machines are well known for their robustness and ease of installation. However, the energy efficiency is lower compared to permanent magnet synchronous machines, in particular in the part load regime at rated flux. This is the case in many standard applications like fans, pumps, and conveyors.

The energy efficiency of induction machines can be increased by appropriately adjusting the flux linkage according to a given operating point. This approach aims at minimizing the energy losses. Many techniques for implementing steady state optimization, which is at a given constant speed and a given constant torque, for induction machines are already available. Such methods can be reviewed, e.g., in [4]. One of these approaches is to search for the optimal operating point [5] or by explicitly solving the optimization problem of minimizing the losses using a machine model [6], when using scalar control. In field oriented control, the optimal flux linkage or equivalently the optimal magnetizing current can be determined using parameter based methods [7,8], search methods [9], or a combination of parameter and search based approaches, as in [10]. Loss minimization for direct torque control was considered in [11]. These methods can be used to increase the energy efficiency in static applications such as heating, ventilation, and air conditioning, pumps, or conveyors.

By increasing the energy efficiency of induction machines, they become more attractive for industrial and electric mobility applications. However, in electric vehicle applications and many industrial applications, motors will be operated in a dynamic regime with continuously changing torque and speed up to the current and voltage limits. An increase in the efficiency of induction machines in dynamic operation will also increase the attractiveness of induction motors for high dynamic servo applications. In this case, the solution of the optimal control problem is more complex for several reasons: In contrast to the optimal control problem for steady state operation, no closed-form solution can be given. As a result, the optimal control problem must be solved online in the inverter at low sampling times. For energy efficient control at varying speed and torque values, the power losses are not constant, but depend on the time varying stator phasor components and the flux linkage dynamics. This dynamic optimization problem is more complex, which requires more computation time.

Numerical offline optimization using dynamic programming was considered in [12–14]. A numerical online solution to the problem is challenging due to the high computational complexity of the problem and the requirement of a low sample time. To cope with these challenges, a model predictive control approach using a parameterized template was proposed in [15], thus simplifying the problem. This approach assumes a particular behavior of the process variables and rewrites the optimal control problem in terms of a parameter optimization problem.

A simple suboptimal online method based on the steady state solution was discussed in [16,17]. An alternative solution based on a filtered flux linkage setpoint in the transient regime was discussed in [18]. In [19,20], polynomial flux linkage prototypes obtained from a numerical solution of the optimization problem were used to reduce losses. In [21], a closed-form solution to the optimization problem based on Pontryagin's principle was proposed. A model predictive control based on state control was developed in [22].

The approaches discussed above do not consider current and voltage limits. These strategies can therefore only be applied in a restricted operating range. Considering these limits requires knowing the behavior of the process quantities in dynamic operation, which can only be determined numerically, e.g., through offline optimization. A strategy for considering these limits was developed in [23]. The method uses general predictive control to solve the optimization problem.

In the cited publications addressing dynamic optimization, iron losses were considered in [12,15,19,20,23], whereas in [16,21], only copper losses were considered. In all cited publications, the optimization interval during dynamic operation of the motor started at the beginning of the torque or speed change.

This paper integrates [24–26], where in contrast to all other approaches, the speed ramp does not start right at the beginning of the optimization interval. The optimization problem does consider the voltage and current limits, as well as the main inductance saturation effect. The obtained optimal offline solution shows that the flux should be increased in an anticipatory manner to the flux in order to minimize losses. The results from the offline optimization procedure are used as a reference trajectory, which now must be achieved with lower computation times, to allow for an online implementation. This is achieved by deriving a template from the results obtained by the offline optimization procedure. The template therefore also considers voltage and current limits, as well as the main inductance saturation effect.

This paper further extends the template based solution by adding a template adaptation algorithm. Using this algorithm, template based flux anticipation is possible. The implementation in an online system becomes feasible, because the offline generated template only needs to be adapted to the current driving situation in the online implementation, which results in significantly lower computation effort compared to the optimization procedure in [24]. This approach is validated, tested, and compared, which is done by simulations and measurements on a test bench. The templated based solution is further compared to a model predictive solution using an online numerical optimization [27]. The benefit of the template based solution in a real-world scenario is illustrated by applying it to the WLTP driving cycle.

This article is structured as follows: Section 2 introduces the machine model used in the following sections. Section 3 describes the optimization problem and its solution. Section 4 presents a simplified approach to obtain an online capable system based on this solution. Simulation and measurement results are given in Sections 6 and 7, respectively. Section 8 demonstrates the benefit of this paper's approach using the WLPT driving cycle. Finally, this article is concluded in Section 9.

2. Modeling

2.1. Machine Model

The machine model parameters in this publication are based on the Γ-inverse equivalent circuit according to [28], as illustrated in Figure 1. $\underline{U}_1$ is the stator voltage phasor, R_1 the stator copper resistance, L_σ the stray inductance, L_μ the main inductance, and R_{Fe} the iron resistance. $\underline{I}_{L_\mu}$ and $\underline{I}_{R_{\mathrm{Fe}}}$ denote the currents through the main inductance and iron resistance, respectively. R_2 is the rotor copper resistance. $\underline{I}_1$ and $\underline{I}_2$ are the stator and rotor current phasors, respectively, and $j\omega_1 L_\mu(\underline{I}_1 + \underline{I}_2)$ is the rotor voltage, with the stator angular frequency ω_1. Note that R_2 does not denote the real, physical rotor resistance, but the referred equivalent value in the Γ-inverse equivalent circuit. This applies to the rotor current $\underline{I}_2$ as well.

This project focuses on induction machines in dynamic operation. This application is typically implemented using a field oriented control method. We consider here field orientation along the rotor flux linkage $\underline{\Psi}_2$. This means that the rotor flux linkage phasor is aligned with the d-axis of a complex reference frame and rotating at speed ω_1. $\Psi_{2\mathrm{d}}$ and $\Psi_{2\mathrm{q}}$ are the rotor flux phasor components. According to [29], the following statement is valid in rotor flux oriented systems:

$$\frac{d\underline{\Psi}_2}{dt} = -j\omega_1\underline{\Psi}_2 + R_{\mathrm{Fe}} I_{R_{\mathrm{Fe}}} \qquad \Rightarrow \qquad I_{R_{\mathrm{Fe}}} = \frac{\frac{d\underline{\Psi}_2}{dt} + j\omega_1\underline{\Psi}_2}{R_{\mathrm{Fe}}}\,. \tag{1}$$

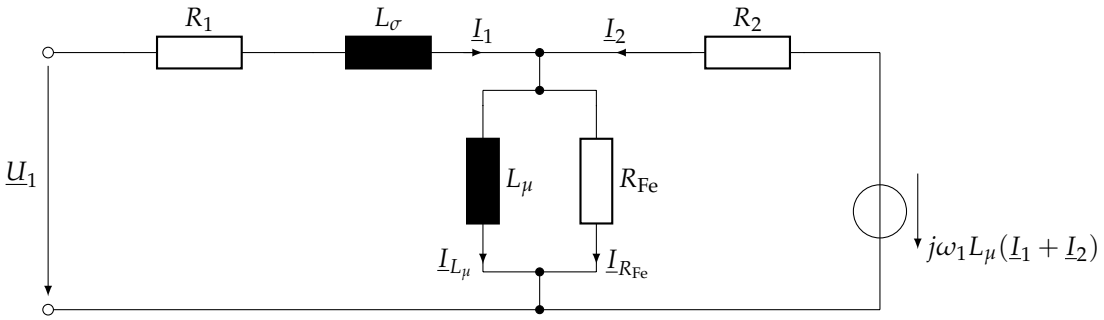

Figure 1. Γ-inverse equivalent circuit of an induction machine including iron resistance.

Based on the equivalent circuit in Figure 1 and knowing the characteristics of (1), the system dynamics in field orientation can be described as follows:

$$\frac{d\Psi_{1\mathrm{d}}}{dt} = -\frac{R_1}{L_\sigma}\Psi_{1\mathrm{d}} + \omega_1\Psi_{1\mathrm{q}} + \frac{R_1}{L_\sigma}\Psi_{2\mathrm{d}} + U_{1\mathrm{d}} \tag{2}$$

$$\frac{d\Psi_{1\mathrm{q}}}{dt} = -\frac{R_1}{L_\sigma}\Psi_{1\mathrm{q}} - \omega_1\Psi_{1\mathrm{d}} + U_{1\mathrm{q}} \tag{3}$$

$$\frac{d\Psi_{2\mathrm{d}}}{dt} = \frac{R_{\mathrm{Fe}}}{R_{\mathrm{Fe}}+R_2}\left(\frac{R_2}{L_\sigma}\Psi_{1\mathrm{d}} - R_2\frac{L_\sigma+L_\mu}{L_\sigma L_\mu}\Psi_{2\mathrm{d}}\right) \tag{4}$$

$$0 = \frac{R_{\mathrm{Fe}}}{R_{\mathrm{Fe}}+R_2}\left(\frac{R_2}{L_\sigma}\Psi_{1\mathrm{q}} - \left(\frac{R_2\omega_1}{R_{\mathrm{Fe}}}+\omega_2\right)\Psi_{2\mathrm{d}}\right). \tag{5}$$

ω_2 denotes the slip angular speed. $\Psi_{1\mathrm{d}}$ and $\Psi_{1\mathrm{q}}$ are the stator flux phasor d- and q-axis components. $U_{1\mathrm{d}}$ and $U_{1\mathrm{q}}$ are the stator d-axis and q-axis voltage phasor components. From (2)–(5), the system current dynamics in continuous time are given as follows:

$$\frac{dI_{1\mathrm{d}}}{dt} = Z_\mathrm{p}\omega_{\mathrm{Rm}}I_{1\mathrm{q}} + \frac{R_2 I_{1\mathrm{q}}^2}{\Psi_{2\mathrm{d}}} - \frac{R_1 I_{1\mathrm{d}}}{\Psi_{2\mathrm{d}}} - \frac{R_{\mathrm{Fe}}}{R_{\mathrm{Fe}}+R_2}\left(\frac{R_2 I_{1\mathrm{d}}}{L_\sigma} - \frac{\Psi_{2\mathrm{d}}}{t_\mathrm{R}L_\sigma}\right) + \frac{U_{1\mathrm{d}}}{L_\sigma} \tag{6}$$

$$\frac{dI_{1\mathrm{q}}}{dt} = -\frac{R_2 I_{1\mathrm{q}} I_{1\mathrm{d}}}{\Psi_{2\mathrm{d}}} - \frac{Z_\mathrm{p}\omega_{\mathrm{Rm}}\Psi_{2\mathrm{d}}}{L_\sigma} - \frac{(R_1+R_2)I_{1\mathrm{q}}}{L_\sigma} - Z_\mathrm{p}\omega_{\mathrm{Rm}}I_{1\mathrm{d}} + \frac{U_{1\mathrm{q}}}{L_\sigma} \tag{7}$$

$$\frac{d\Psi_{2\mathrm{d}}}{dt} = \frac{R_{\mathrm{Fe}}}{R_{\mathrm{Fe}}+R_2}\left(R_2 I_{1\mathrm{d}} - \frac{\Psi_{2\mathrm{d}}}{t_\mathrm{R}}\right) \tag{8}$$

$$\frac{d\omega_{\mathrm{Rm}}}{dt} = \frac{T_{\mathrm{Mi}} - T_\mathrm{L}}{J_\mathrm{M}+J_\mathrm{L}}. \tag{9}$$

Z_p denotes the number of pole pairs of the machine. ω_{Rm} is the shaft mechanical angular speed with $\omega_{\mathrm{Rm}} = (\omega_1 - \omega_2)/Z_\mathrm{p}$. $I_{1\mathrm{d}}$ and $I_{1\mathrm{q}}$ are the stator current phasor components. t_R is the rotor time constant defined as $t_\mathrm{R} = L_\mu/R_2$. J_M and J_L are the motor and load inertia, respectively. The variable:

$$T_{\mathrm{Mi}} = \frac{3}{2}Z_\mathrm{p}\Psi_{2\mathrm{d}}I_{1\mathrm{q}} \tag{10}$$

represents the torque produced by the machine. T_L denotes the load torque applied to the machine. Currents and voltages in this paper are represented using the amplitude invariant scaling of the Clarke transformation.

2.2. Main Inductance Saturation

The modeling of a real induction machine must consider the nonlinear characteristic of the machine's magnetic circuit. The machine parameters are dependent on the operating point. This paper considers the main inductance saturation effect. The main inductance L_μ

at a given magnetizing current I_{1d} is measured for the motor under test given as in Figure 2 as an example for a motor with a rated power of 370 W.

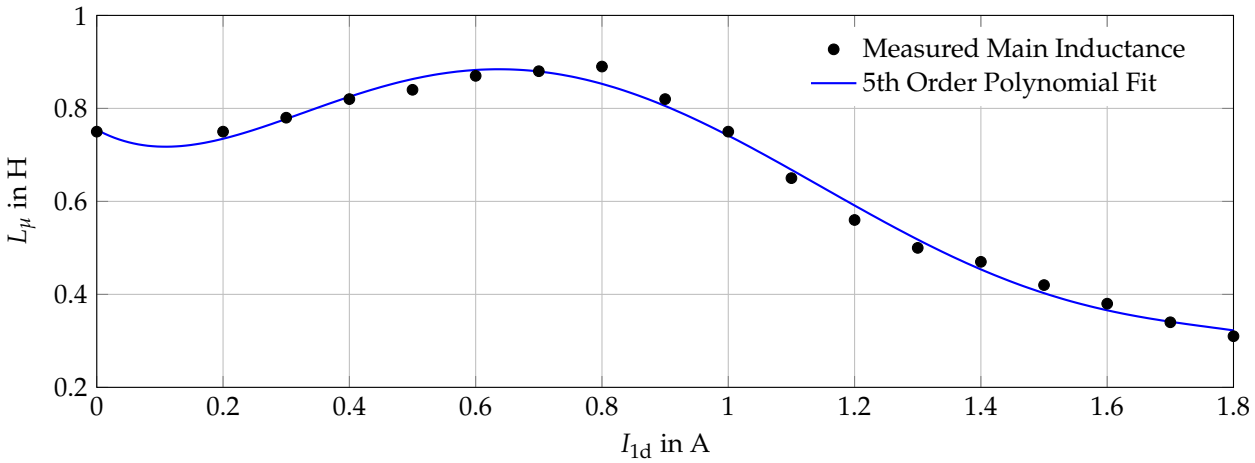

Figure 2. Measured main inductance values and polynomial fit to these values.

Then, to obtain an analytical representation, a polynomial function is fit to the main inductance data points using the `Curve Fitting Toolbox` from MATLAB. A reasonably good approximation is obtained by a fifth order polynomial model (11) of the main inductance as a function of the magnetizing current I_{1d}, whose coefficients for the considered motor with a rated power of *SI370W* are given in Table A1:

$$L_\mu(I_{1d}) = a_5 I_{1d}^5 + a_4 I_{1d}^4 + a_3 I_{1d}^3 + a_2 I_{1d}^2 + a_1 I_{1d} + a_0 \,. \tag{11}$$

The main inductance curve is given by $L_\mu(I_{1d})$ for $0 \leq I_{1d} \leq I_{1,max}$. Thus, the steady state flux is given by $\Psi_2 = L_\mu(I_{1d}) I_{1d}$ and the rotor time constant $t_R = L_\mu(I_{1d})/R_2$.

2.3. Loss Model

To evaluate the power losses, a loss model must be developed. The power loss Equation (12) includes both the constant power loss in the steady state operation of the machine, as well as the transient power losses [16] and iron losses considering the main inductance saturation effect in continuous time:

$$P_L = \underbrace{\frac{3}{2}R_1(I_{1d}^2 + I_{1q}^2) + \frac{3}{2}R_2(I_{1d}^2 + I_{1q}^2)}_{\text{Static losses}} + \underbrace{\frac{3}{2}R_2\left(\frac{\Psi_2^2}{L_\mu^2(I_{1d})} - 2\frac{\Psi_2 I_{1d}}{L_\mu(I_{1d})}\right)}_{\text{Dynamic losses}} + \underbrace{\frac{3}{2}R_{Fe}I_{R_{Fe}}^2}_{\text{Iron losses}}, \tag{12}$$

where $I_{R_{Fe}}^2$ is given by [29] and (1) when considering $\Psi_{2q} = 0$ in rotor flux orientation as follows:

$$I_{R_{Fe}}^2 = \left(\frac{\dot{\Psi}_{2d}}{R_{Fe}}\right)^2 + \left(\frac{\omega_1 \Psi_{2d}}{R_{Fe}}\right)^2 .$$

2.4. Influence of Iron Losses

An induction machine has more sources of power losses than the copper and iron resistances, e.g., friction, but these two are considered to be the main contributors. A modeling of all losses would therefore only exhibit minor benefits, but increase the problem's complexity. In order to achieve reasonably short computation times, the optimization problem must be as simple as possible. The iron resistance is assumed to be of little relevance for dynamic optimization. It will therefore be neglected and considered to be infinite in the

following optimization procedures. However, this assumption needs to be justified by the simulation results given in Section 6.2.

3. Optimization Procedure

3.1. Optimal Control Problem

The objective of this paper is the optimization of motor energy efficiency for dynamic operation, that is for changing load torques and/or for changing speeds. To evaluate the effect of changing speeds, a speed ramp $\omega_{\mathrm{Rm,ref}}(t)$ in an interval $t \in [t_0 \quad t_\mathrm{f}]$ is considered. In contrast to the efficiency optimization methods for steady state operation, the power losses will not be constant in the considered time interval. Therefore, the efficiency must be evaluated based on the overall energy losses. In addition, the speed must closely match the reference speed trajectory. The speed deviation therefore must also be considered in the objective functional, which is formulated as follows:

$$J = \int_{t_0}^{t_\mathrm{f}} \left(\left(P_\mathrm{L}(t) + q \left(\omega_\mathrm{Rm}(t) - \omega_\mathrm{Rm,ref}(t) \right) \right)^2 \right) dt \, . \tag{13}$$

The variable q represents a weighting factor in $\mathrm{W}/(\mathrm{rad\,s^{-1}})^2$ for specifying optimization priorities. The impact of this factor is discussed in Section 3.3.

The optimal control problem must consider the current, flux, and speed dynamics (6)–(9), the equality constraint with respect to the torque (10), and the inequality constraints (14):

$$\sqrt{U_\mathrm{1d}^2 + U_\mathrm{1q}^2} \leq U_\mathrm{1,max} \qquad\qquad \sqrt{I_\mathrm{1d}^2 + I_\mathrm{1q}^2} \leq I_\mathrm{1,max} \, , \tag{14}$$

where $U_\mathrm{1,max}$ is the maximum length of the inverter output voltage phasor, which depends on the DC link voltage. The variable $I_\mathrm{1,max}$ represents the current limit given by the minimum of the inverter and motor current limits.

Due to the nonlinear nature of the objective functional (13), the system of Equations (6)–(10), as well as the constraints (14), the optimization problem will be solved using a sequential programming method to find the minimum of the constrained nonlinear multivariable function.

3.2. Implementation

The implementation of dynamic trajectory optimization requires the consideration of system state dynamics as constraints along with the boundary conditions. In the implementation of the problem, the `fmincon` solver from MATLAB is used. For the implementation, the continuous time system dynamics (6)–(9) are discretized with the sample time t_s and $t = kt_\mathrm{s}$. The state discretization is implemented using the Runge–Kutta fourth order method. From the discretization of the objective functional (13), the discretized performance index J_d is obtained:

$$J_\mathrm{d} = \sum_{k=1}^{N} P_\mathrm{L}(k) + q \sum_{k=1}^{N} \left(\omega_\mathrm{Rm}(k) - \omega_\mathrm{Rm,ref}(k) \right)^2 . \tag{15}$$

$P_\mathrm{L}(k)$ is the discretized instantaneous power loss from (12). $\omega_\mathrm{Rm,ref}(k)$ is the reference speed trajectory of the rotor at the sampling instants. By substituting the power loss Equation (12) in (15) and considering $I_{R_\mathrm{Fe}} = 0$, we obtain the discretized performance index (16). N is the total number of samples.

The `fmincon` solver attempts to find the control variables, that is the stator voltage phasor components, such that the value of the objective functional J_d is minimized, subject to the given constraints and the initial guess. The initial guess is determined by the given initial state. Assuming that the motor is in a steady state prior to the speed ramp, the initial values for the currents, flux, and voltage trajectories can be determined based on a steady state optimization procedure as given in the literature. The boundary conditions (14)

are rewritten as nonlinear inequality constraints. The optimization procedure is then performed using the motor parameters given in Table A1.

$$J_\mathrm{d} = \sum_{k=1}^{N} \left(\frac{3}{2}(R_1 + R_2)\left(I_{1\mathrm{d}}^2(k) + I_{1\mathrm{q}}^2(k)\right) + \frac{3}{2}R_2\left(\frac{\Psi_2^2(k)}{L_\mu^2(I_{1\mathrm{d}})} - 2\frac{\Psi_2(k)I_{1\mathrm{d}}(k)}{L_\mu(I_{1\mathrm{d}})}\right)\right) + q\sum_{k=1}^{N}\left(\omega_\mathrm{Rm}(k) - \omega_\mathrm{Rm,ref}(k)\right)^2 \tag{16}$$

3.3. Optimal Offline Solution

Figure 3 illustrates the results obtained by offline solving the problem given above in Section 3.1. The figure displays the solution to the optimization problem with the given parameters. In conventional approaches such as [15–17,21], the optimization interval is chosen in such a way that the torque step occurs at the beginning of the optimization interval, that is at time $t = 0$. In contrast, the main idea of this paper is to modify the optimization interval such that the torque step occurs later in the optimization interval at time $t > 0$. At $t = 0.4\,\mathrm{s}$, the speed ramp command is given, which results in a torque step. Note that the flux Ψ_2 is low at the beginning of the optimization interval due to the low required torque at the steady state initial condition. This corresponds to the well-known results from steady state optimization. Although the speed command is only triggered at $t = 0.4\,\mathrm{s}$, the optimization algorithm can already modify the flux for $t \in [0 \quad t_1]$, thus anticipating the flux increase based on the knowledge of the torque and speed profile. At $t = 0.4\,\mathrm{s}$, the flux Ψ_2 has already started to increase. The figure indicates that operation at the voltage limits, as well as in the field weakening regime is possible. This can be seen at $t = 0.75\,\mathrm{s}$, where $U_{1\mathrm{d}}$ reaches its limit.

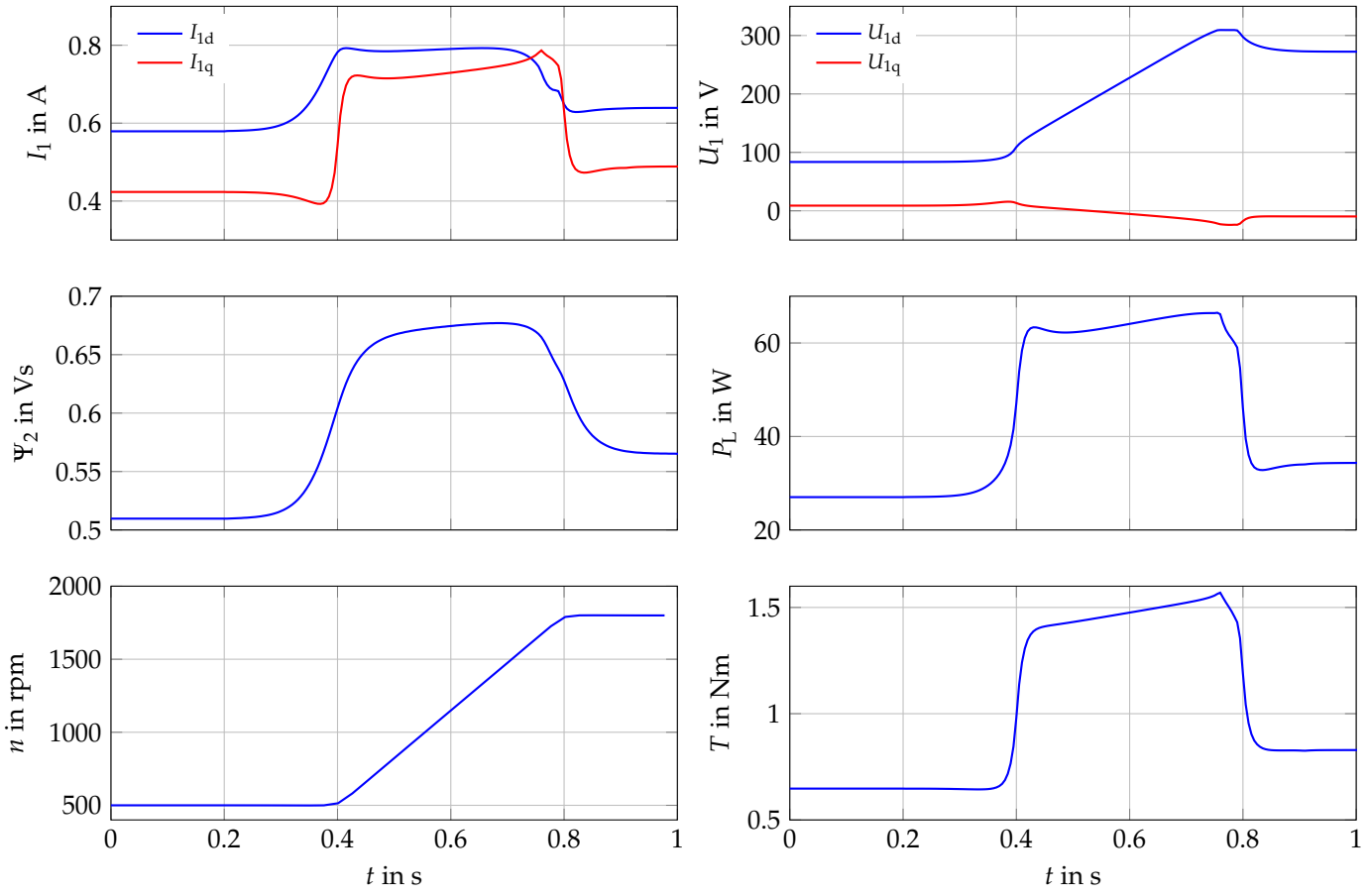

Figure 3. Offline optimization results.

The parameter q was selected to be $q = 1\,\mathrm{W/(rad\,s^{-1})^2}$ based on previous experience with objective functionals of numerical optimizations. To illustrate that this selection is reasonable, a simulation study was conducted, where the procedure described in this section was executed multiple times for various values of q. Figure 4 shows a comparison of three optimizations results. The left plot of Figure 4 displays the speed reference $\omega_{\mathrm{Rm,ref}}$ given as a constraint to the optimization procedure. For $q = 5\,\mathrm{W/(rad\,s^{-1})^2}$, which elevates the speed accuracy over the energy efficiency, the speed trajectory obtained by the optimization is closest to $\omega_{\mathrm{Rm,ref}}$. For $q = 0.2\,\mathrm{W/(rad\,s^{-1})^2}$, which elevates energy efficiency over speed accuracy, the speed trajectory obtained by the optimization shows some deviation at the beginning and ending of the speed ramp. For $q = 1\,\mathrm{W/(rad\,s^{-1})^2}$, the speed trajectory lies in between. The middle and right plot of Figure 4 show the corresponding power losses and energy consumption for each of these cases. As expected, the power losses are highest for $q = 5\,\mathrm{W/(rad\,s^{-1})^2}$ and lowest for $q = 0.2\,\mathrm{W/(rad\,s^{-1})^2}$.

This demonstrates how the factor q can be selected according to the given priorities of the desired application. The selected value of $q = 1\,\mathrm{W/(rad\,s^{-1})^2}$ displays a reasonable tradeoff between speed accuracy and energy efficiency.

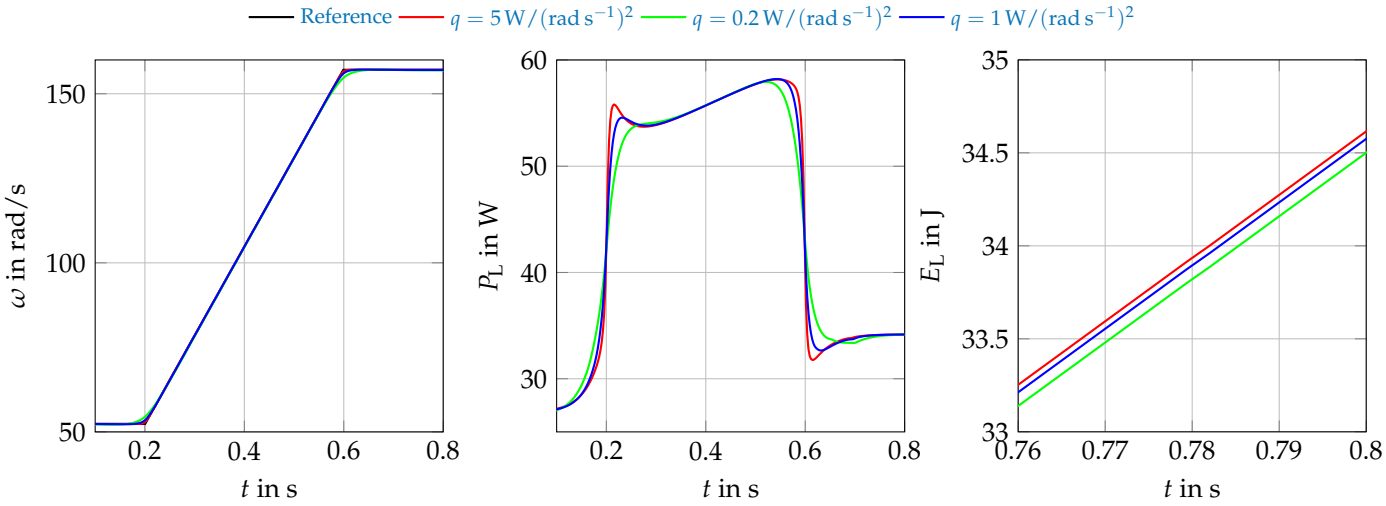

Figure 4. Offline optimization results for different values of q.

These optimization results show that the `fmincon` solver increases the flux Ψ_2 prior to the torque step. The currents $I_{1\mathrm{d}}$ and $I_{1\mathrm{q}}$ therefore do not increase at the same time, which decreases the power losses. This observed flux trajectory suggests that modifying the flux in an anticipative manner to the required torque is beneficial for minimizing power losses in dynamic operation, which will be verified in Section 7.2.

4. Template Based Solution

The optimal offline solution found in the previous section required a significant computation time, which does not allow for real-time operation. Of course, this amount of time will not be available in any microprocessor of a standard frequency inverter. In this section, the optimal offline solution will be considered as a reference. Because of the high computation effort, the optimal flux trajectory is approximated. A template that resembles the shape of the optimal flux trajectory is therefore derived from the offline optimal solution. The main advantage of using a template is the low computation effort, which allows for an easy online implementation and retrofitting of existing drive systems. The generation of such templates and the adaptation to a specific driving situation will be presented in the following subsections.

4.1. Template Generation

To generate the flux template, a torque profile T_{ref} given in the lower part of Figure 5 is considered. Using the optimization procedure from Section 3, the optimal flux trajectory $\Psi_{2,\mathrm{opt}}$ is calculated. The optimal flux trajectory is displayed in the upper part of Figure 5. The solver increases the rotor flux linkage in an anticipative manner in the interval $t \in [t_{\Psi_2} \quad t_{\mathrm{T}_2}]$. A numerical analysis given in Section 6.1 needs to be conducted to estimate the anticipation time interval $\Delta t_{\mathrm{a}} = t_{\mathrm{T}_2} - t_{\Psi_2}$. It is expected to be linked to the rotor time constant t_{R}. Based on the results from Section 3.3, it can be assumed to be in the range of $\Delta t_{\mathrm{a}} = \in [2t_{\mathrm{R}} \quad 3t_{\mathrm{R}}]$.

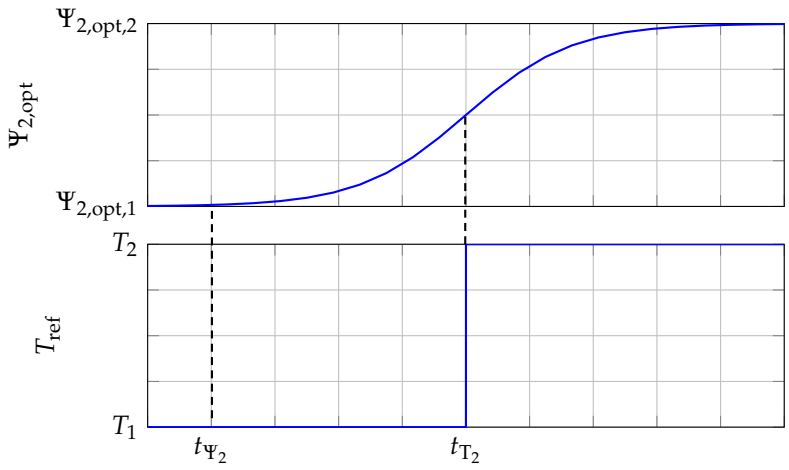

Figure 5. Torque profile T_{ref} and corresponding optimal rotor flux $\Psi_{2,\mathrm{opt}}$.

This knowledge can be used to extract a general template $\Psi_{2,\mathrm{template}}$ (17). Assume that an optimal flux linkage trajectory $\Psi_{2,\mathrm{opt}}$ as illustrated in the upper part of Figure 5 was determined for a particular torque trajectory given in the lower part of Figure 5. Then, from this curve, the normalized flux linkage template is determined by:

$$\Psi_{2,\mathrm{template}} = \frac{\Psi_{2,\mathrm{opt}} - \Psi_{2,\mathrm{opt},1}}{\Psi_{2,\mathrm{opt},2} - \Psi_{2,\mathrm{opt},1}} \tag{17}$$

such that $\Psi_{2,\mathrm{template}} \in [0 \quad 1]$. This template can be stored as a lookup table.

When considering a torque step from T_1 to T_2, the steady state optimal magnetizing current can be determined by numerically solving the equation:

$$I_{1\mathrm{d}} = \frac{4}{9}\frac{(R_1 + R_2)}{R_1}\frac{T^2}{Z_{\mathrm{p}}^2 L_\mu^2(I_{1\mathrm{d}})}\left(\frac{1}{I_{1\mathrm{d}}^3} + \frac{1}{I_{1\mathrm{d}}^2 L_\mu(I_{1\mathrm{d}})}\frac{\partial L_\mu}{\partial I_{1\mathrm{d}}}\right)$$

for $T = T_1$ and $T = T_2$. The results are the optimal steady state magnetizing currents $I_{1\mathrm{d},\mathrm{opt},\infty}(T_1)$ and $I_{1\mathrm{d},\mathrm{opt},\infty}(T_2)$. Using these values, the steady state optimal flux linkage values:

$$\Psi_{2,\mathrm{opt},\infty}(T_1) = L_\mu I_{1\mathrm{d},\mathrm{opt},\infty}(T_1) \qquad \Psi_{2,\mathrm{opt},\infty}(T_2) = L_\mu I_{1\mathrm{d},\mathrm{opt},\infty}(T_2)$$

can be calculated. The flux linkage trajectory $\Psi_{2,\mathrm{opt}}$ for the torque step from T_1 to T_2 is calculated by rescaling the normalized template $\Psi_{2,\mathrm{template}}$ from (17) as follows:

$$\Psi_{2,\mathrm{opt}} = \Psi_{2,\mathrm{opt},\infty}(T_1) + \Delta\Psi_2 \Psi_{2,\mathrm{template}} \quad \text{where} \quad \Delta\Psi_2 = \Psi_{2,\mathrm{opt},\infty}(T_2) - \Psi_{2,\mathrm{opt},\infty}(T_1)\,.$$

The overall procedure is summarized in Figure 6. Note that the optimal steady state magnetizing current $I_{1\mathrm{d},\mathrm{opt},\infty}(T)$ can be either determined during the online procedure or calculated offline and stored as a lookup table as well.

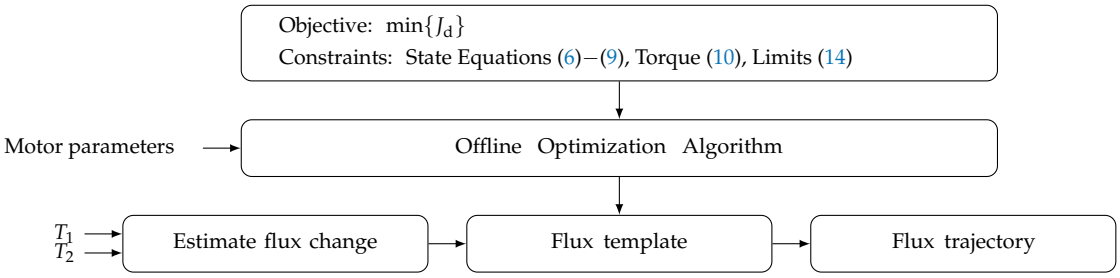

Figure 6. Flux template generation procedure.

Figure 7 illustrates flux linkage templates generated with the method mentioned above for the motor described in Table A1. The flux linkage trajectories generated for various load torque steps are compared to the offline optimal flux linkage trajectory generated from the solution of the optimization problem in Section 3.1 considering the anticipative flux linkage rise time. It can be observed that both methods yield similar results. At higher torque steps, the offline optimal flux linkage trajectory for this motor deviates slightly from the trajectories generated by the template.

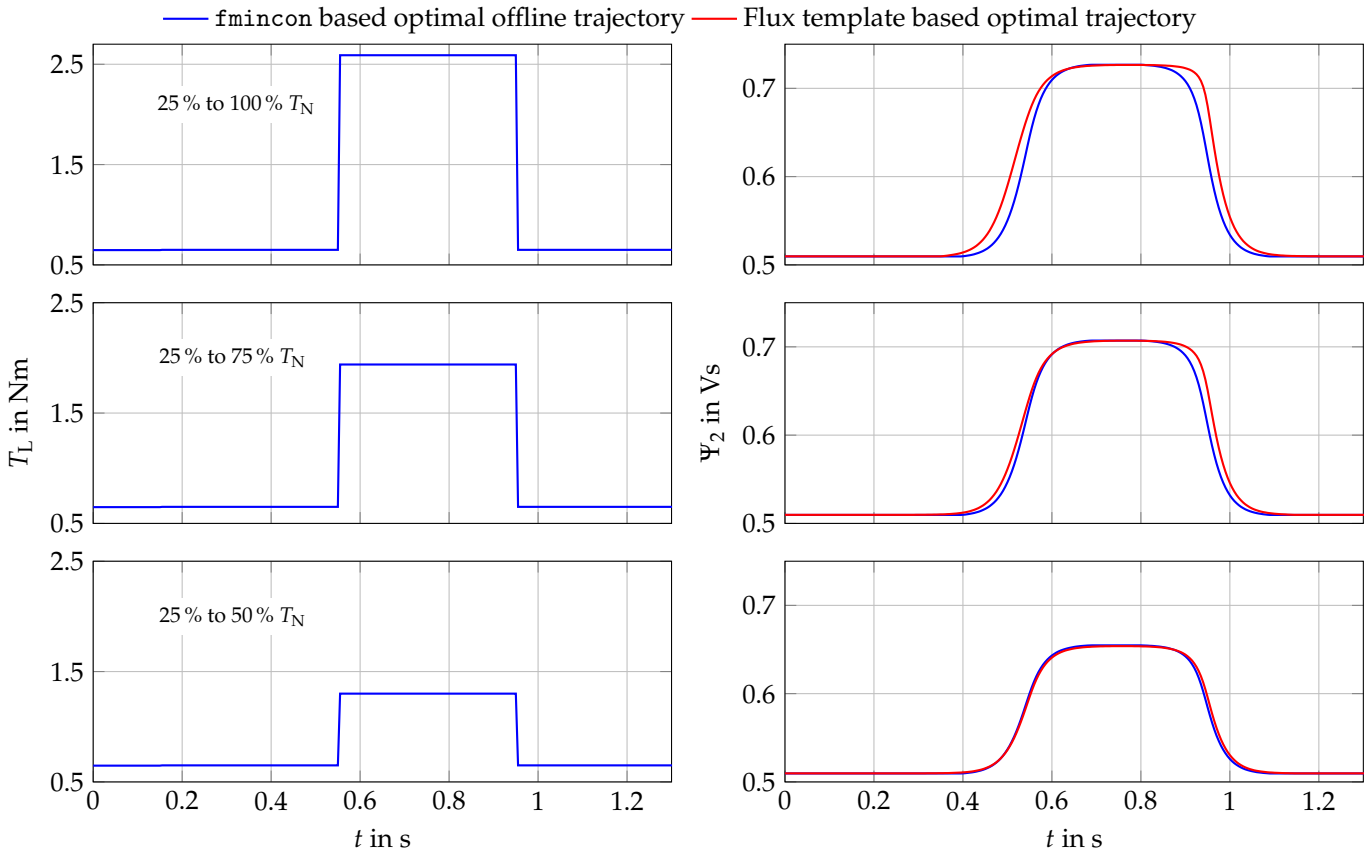

Figure 7. Flux trajectories for the motor specified in Table A1 for different torque steps.

4.2. Template Adaptation

The template generation algorithm presented in the section above is only capable of processing individual speed ramps. In order to be used in a more general setup, where the machine is continuously accelerating and decelerating, the template generation must be combined with an adaptation algorithm.

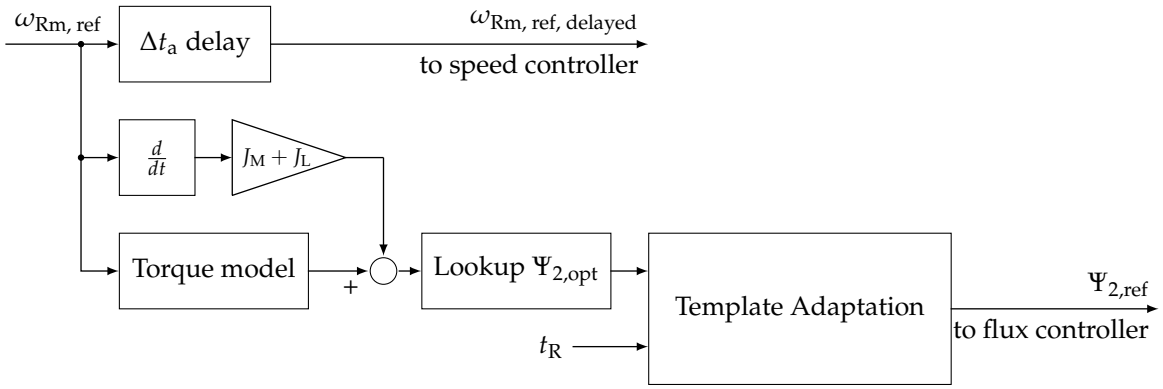

Figure 8. Template adaptation scheme.

As displayed in Figure 8, the template adaptation algorithm will first delay the speed reference signal by the anticipative delay time Δt_{a} in order to achieve flux anticipation. Using the undelayed speed reference signal and a torque prediction model, the according optimal steady state flux is calculated. Due to the template generation procedure, the optimal steady state flux is automatically applied in steady state operation. If this optimal steady state flux changes significantly, a template generation is triggered, because a transient state has been detected. The template generation will then adapt to the new optimal steady state flux. If a template generation is triggered before the previous template trajectory was fully completed, the old template generation is aborted. A new template generation is started that meets two requirements: First, the final value of the new template generation matches the required optimal steady state flux. Second, the transition from one template generation to the next is continuous.

The result of the template adaptation algorithm is shown in Figure 9. The upper plot displays the speed reference in real-time and the delayed signal, which is passed to the speed controller. In the middle plot, the required torque is displayed. The torque is estimated based on the speed reference using a linear friction model for simplicity together with 0.1 Nm of the static torque component starting from $t = 0.05\,\mathrm{s}$ and a torque profile generation based on the a priori inertia J_{M} and J_{L}. Based on the required torque, the optimal steady state flux is given in the bottom plot. Note that the slope of this trajectory continuously changes in contrast to the previous section. At time $t = 0.2\,\mathrm{s}$, it can be seen that the template adaptation algorithm adapts to the beginning of the torque ramp. The previous template was not yet finished, but the transition to the new template generation is smooth. The template reaches the desired steady state flux value during the ramp, although there is a changing slope at $t = 0.21\,\mathrm{s}$. The template adaptation algorithm is further able to adapt to the rising friction torque during the speed ramp, as can be seen in $t \in [0.5 \quad 0.7]\,\mathrm{s}$.

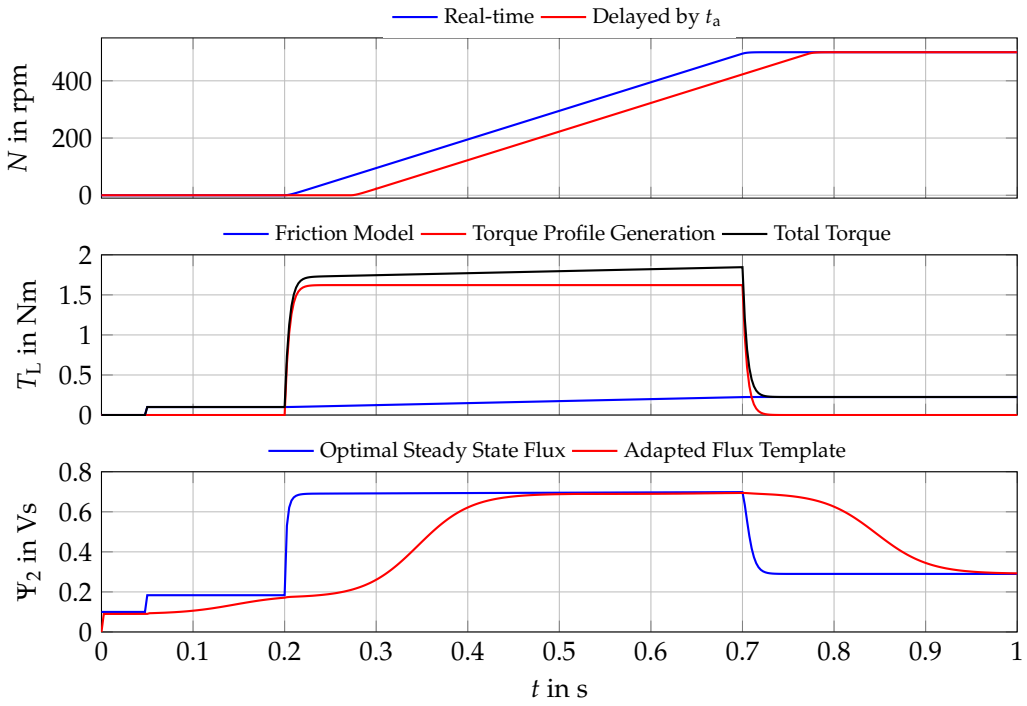

Figure 9. Trajectories generated by the template adaptation algorithm.

5. Model Predictive Solution

A different approach to minimizing energy losses in dynamic operation is to implement a model predictive online optimization. This approach requires more computation time than a template. It can therefore only be used in high sample time systems. The model predictive solution will be used to compare the template based solution to an existing online optimization method.

The model predictive solution was implemented online using the software package GRAMPC [27]. The optimal control problem in Section 3.1 is formulated such that the copper losses are minimized during the transient operation. The copper losses are minimized subject to voltage and current limit constraints. The effect of main inductance saturation is also included. The optimal control algorithm using GRAMPC was implemented using MATLAB/Simulink and dSPACE. Measurements on a 370 W motor are given in Section 7. In order to implement an online optimization using GRAMPC, the state Equations (6)−(9) including the main inductance saturation effect (11) must be represented as Jacobians. The optimizer must consider the voltage and current limits (14). These constraints are rewritten as nonlinear inequality constraints and normalized by their respective maximum value. The integral cost is equivalent to the objective function (15).

6. Simulations

To verify the proposed template based solution, a simulation environment was set up. The simulation consisted of two main parts: the motor model as described in Section 2 and the field oriented control, as shown in Figure 10 in a simplified form. The speed controller commands a torque T_{ref}. Based on the flux linkage $\Psi_{2,\mathrm{act}}$, which is estimated using the magnetizing current with a simple first order model, the reference for the quadrature current $I_{1\mathrm{q,ref}}$ was calculated. The reference $I_{1\mathrm{d,ref}}$ for the magnetizing current is given by the flux controller output. $\Psi_{2\mathrm{d,ref}}$ corresponds to the values calculated in the optimization procedures as described in the sections before.

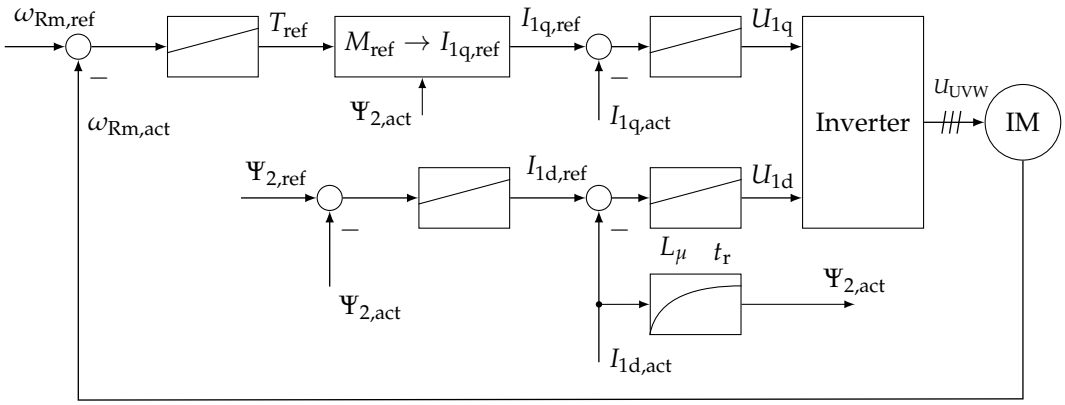

Figure 10. Control structure.

6.1. Template Generation

In order to generalize the approach to different motor sizes, a numerical study will be given in the sequel. This study will determine whether the optimal flux trajectory depends on motor size and torque steps and find the value of the anticipation time Δt_a. The optimization procedure described in Section 3 was therefore conducted multiple times for different motor parameters and speed ramps.

Figure 11 shows the results for different motor sizes. Starting from a given motor speed $\omega_{\mathrm{Rm},1}$ and given load torque T_L, at time $t = t_1$, a speed ramp to $\omega_{\mathrm{Rm},2}$ in the interval $t \in [t_1 \quad t_2]$, $t_1 \geq 0$ and $t_2 \leq t_\mathrm{f}$ is commanded. The MATLAB `fmincon` solver generates optimal flux and current trajectories subject to minimizing the objective functional (15). It can be observed that in the optimal solution, the flux increases prior to the torque. A deeper analysis shows that the anticipation time Δt_a for different motor sizes increases with the rotor time constant. The overall shape of the optimal flux trajectory does not change significantly for different motors. The relationship between the torque step size and the flux rise anticipation time is analyzed based on the motor from Figure 11 with a rated power of 370 W in Figure 12. It can be observed that the anticipative flux rise time does not significantly depend on the torque levels. The flux weakening during speed ramps above the rated speed to satisfy the voltage limit constraint can also be observed from this result. The optimal anticipation time is found to be $\Delta t_\mathrm{a} = 2.5 t_\mathrm{R}$.

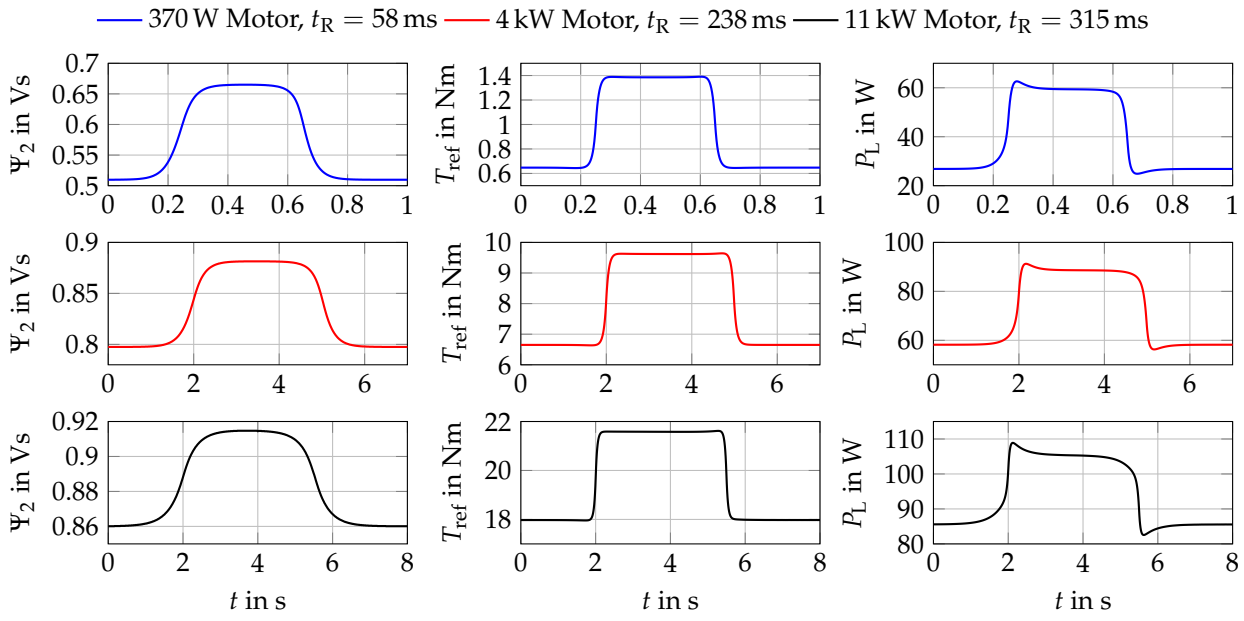

Figure 11. Simulation of optimal flux trajectories and torque for various motor sizes.

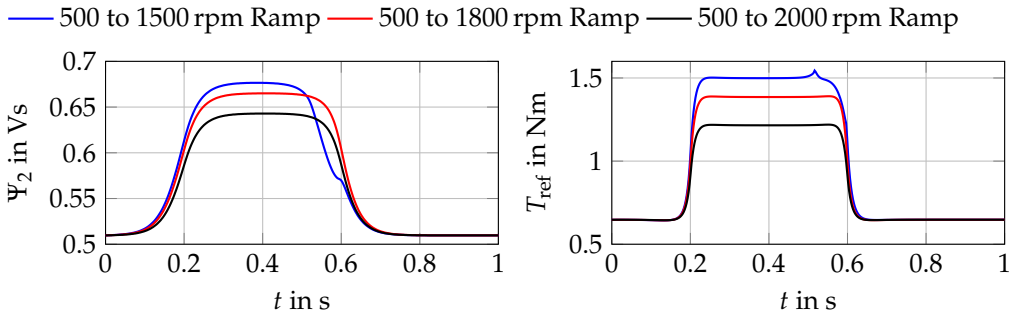

Figure 12. Simulation of optimal flux trajectories and torque for different torque steps for a 370 W motor.

6.2. Influence of Iron Losses

In Section 2.4, we discussed why iron losses are neglected in this article. To illustrate that this simplification does not significantly affect the optimization procedure for dynamic operation given in Section 3, a simulation study is presented. In this study, the optimal flux trajectory is applied to a motor model including iron losses and to a model not including iron losses. The resulting power losses according to (12) are compared in Figure 13.

The losses are calculated for a 0.4 s speed ramp from 500 rpm to 1500 rpm starting at $t = 0.2$ s and the flux trajectory corresponding to the 370 W motor in Figure 11. As the iron losses are flux dependent, the losses will also increase due to this particular flux linkage trajectory. It can be observed that the iron losses are higher at high speeds, thus resulting in high losses at the end of ramp period. However, in the interval $t \in [0.05s \quad 0.2s]$, that is within the anticipation time Δt_{a}, the difference between the simulated losses without considering the iron losses and the simulated losses with consideration of the iron losses is almost constant. Thus, it can be concluded that the effect of the anticipative flux rise on the iron losses is not significant. In principle, iron losses could be included in the optimization procedure and template generation. However, this would increase the complexity significantly for two reasons. First, the template will then also depend on the speed. Second, the template adaptation algorithm Section 4.2 must consider the speed as well. Thus, the main benefit of this method, its simplicity, is no longer provided.

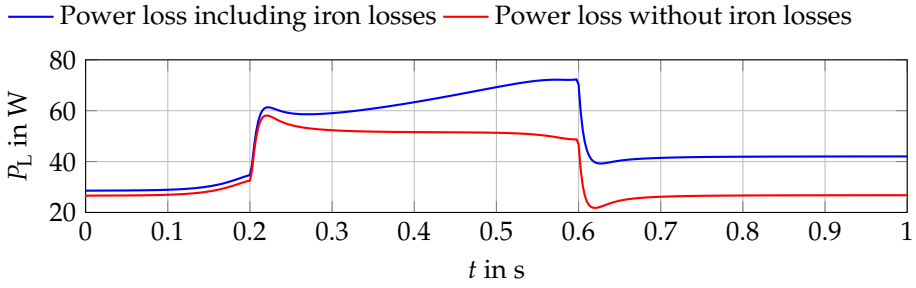

Figure 13. Simulation of power losses including iron losses and without iron losses.

7. Measurements

The procedure described in the previous sections is now substantiated by measurements using the test bench illustrated in Figure 14. The obtained results are then compared to measurements for the rated flux operation and also with the sub optimal results from [16]. The load was provided by a permanent magnet synchronous machine controlled by a standard inverter. The control of the induction machine was implemented on a dSPACE ds1104 rapid prototyping system, which controlled the PWM signals of a modified standard inverter. The torque and speed were measured using a torque sensor with an integrated encoder. To compensate a possible offset, the sensor was automatically calibrated to zero upon startup. All signals were recorded using the rapid prototyping system. The power losses were calculated based on the recorded voltage and current values for all three phases, as well as the torque and speed signals.

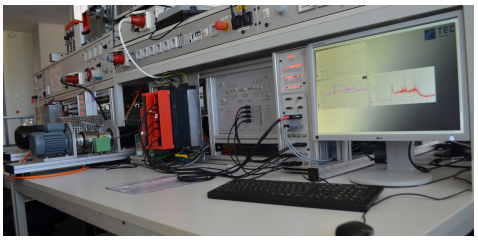

Figure 14. Test bench.

7.1. Optimal Offline Solution

This section illustrates results obtained by the optimization procedure given in Section 3. Starting from a given motor speed $\omega_{\mathrm{Rm},1}$ and a given load torque T_{L}, at time $t = t_1$, a speed ramp to $\omega_{\mathrm{Rm},2}$ in the interval $t \in [t_1 \quad t_2]$, $t_1 \geq t_0$, and $t_2 \leq t_{\mathrm{f}}$ is commanded. The load torque is not constant, and the frictional torque components are added to the load torque in the offline optimization process. The considered motor has a rated power of $P_{\mathrm{N}} = 370\,\mathrm{W}$, rated torque $T_{\mathrm{N}} = 2.59\,\mathrm{Nm}$ and a rated speed of $n_{\mathrm{N}} = 1370\,\mathrm{rpm}$. The motor parameters are specified in Table A1. The moment of inertia J_{M} given in Table A1 represents the overall moment of inertia of the induction machine and the load motor, as well as the couplings between the two motors and the torque sensor. Note that the final motor speed $\omega_{\mathrm{Rm},2}$ was selected such that field weakening will be necessary to consider the voltage limit. The given load torque is represented in (18). The torque at the initial speed $\omega_{\mathrm{Rm},1}$ is selected as 25% of the rated motor torque and for final speed $\omega_{\mathrm{Rm},2}$ is taken as 25% + 7% of rated motor torque. The additional 7% accounts for the torque due to friction at the final speed. The load torque transition from the initial to the final value is assumed to be linear for simplicity. The results illustrate the behavior in the field weakening regime as well.

$$T_{\mathrm{L}} = \begin{cases} 25\,\%\,T_{\mathrm{N}}, & \omega_{\mathrm{Rm}} = \omega_{\mathrm{Rm},1} \\ C_1\,\omega_{\mathrm{r}} + C_2\,, & \omega_{\mathrm{Rm},1} \leq \omega_{\mathrm{Rm}} \leq \omega_{\mathrm{Rm},2} \\ (25\,\% + 7\,\%)\,T_{\mathrm{N}}, & \omega_{\mathrm{Rm}} = \omega_{\mathrm{Rm},2} \end{cases} \tag{18}$$

Figure 15 illustrates the results obtained by applying the offline calculated optimal trajectory from Section 3 for $I_{1\mathrm{d}}$ during the considered speed trajectory as a reference value. It can be noted that during the speed ramp, the magnetizing current trajectory in the optimal case corresponds to the trajectory obtained in the previous section. The slight mismatch in the quadrature current can be attributed to neglecting of iron losses in the power loss model and the simplified modeling of friction torque. Figure 16 shows the power loss measurements of various cases with that of the optimization result in Figure 3.

In addition, in Figure 16, a comparison of the loss energy, that is the integration of the power losses for the considered speed profile, is shown for the optimal trajectory. The result is compared to the one obtained for an operation with rated flux linkage, that is without optimization and for the suboptimal operation from [16]. The power loss is integrated for a time interval during which the dynamic operation of the motor occurs $t \in [0.2\,\mathrm{s} \quad 1.2\,\mathrm{s}]$. In the first time interval $t \in [0.2\,\mathrm{s} \quad 0.4\,\mathrm{s}]$, the loss energy increases slower for the optimal flux linkage, which is an expected result. In the second interval for $t \in [0.4\,\mathrm{s} \quad 0.8\,\mathrm{s}]$, the loss energy increases. This is due to the higher magnetizing and quadrature current required for increasing the flux linkage to the new optimal value and obtaining the required torque at initially lower flux linkage. This increase in P_{L} can also be observed in the corresponding plot in Figure 16. This particular effect motivates the need for optimization in this situation to reduce the losses as much as possible. Finally, the loss energy for the operation with optimal flux linkage is lower than the loss energy obtained for rated flux linkage and the suboptimal case. This demonstrates the benefit of using the optimization procedure. The abnormal result towards the end of the speed ramp for the suboptimal case is because of the limitations of [16] in which the voltage and current limits were not considered.

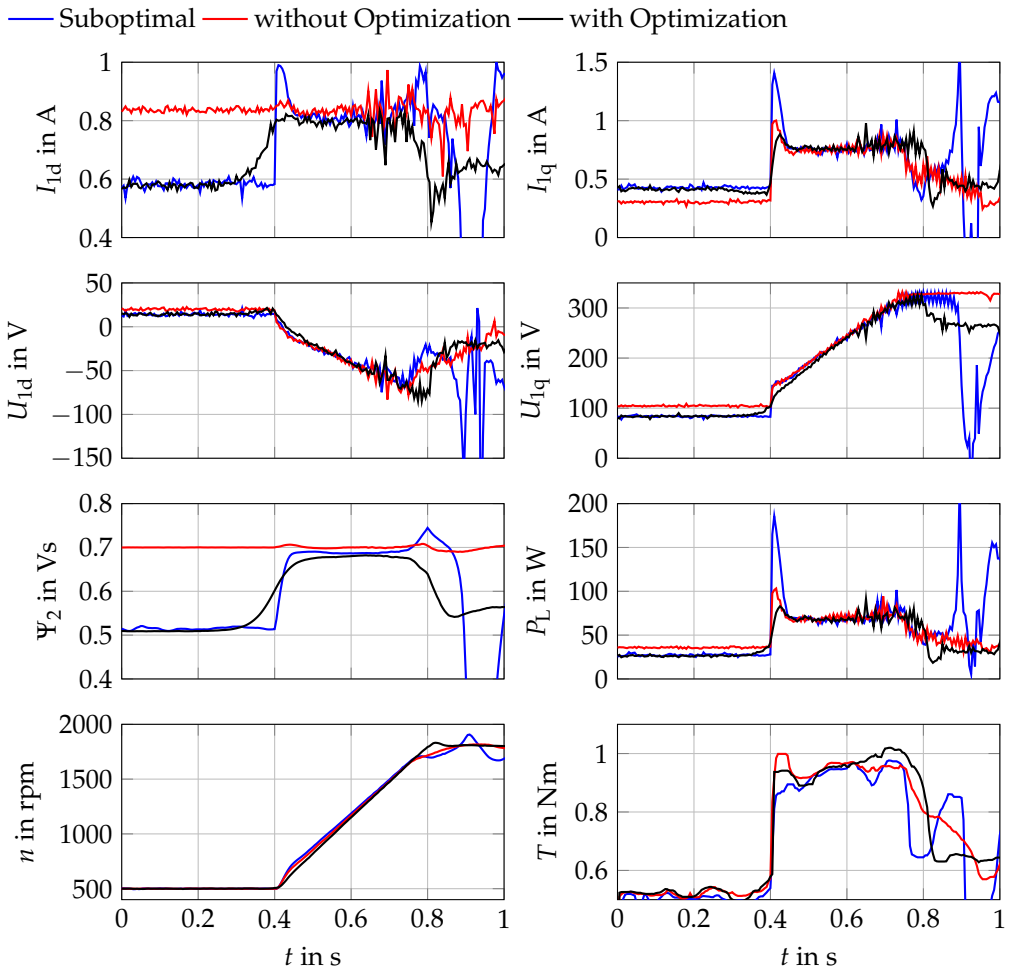

Figure 15. Measurement results for the optimization procedure.

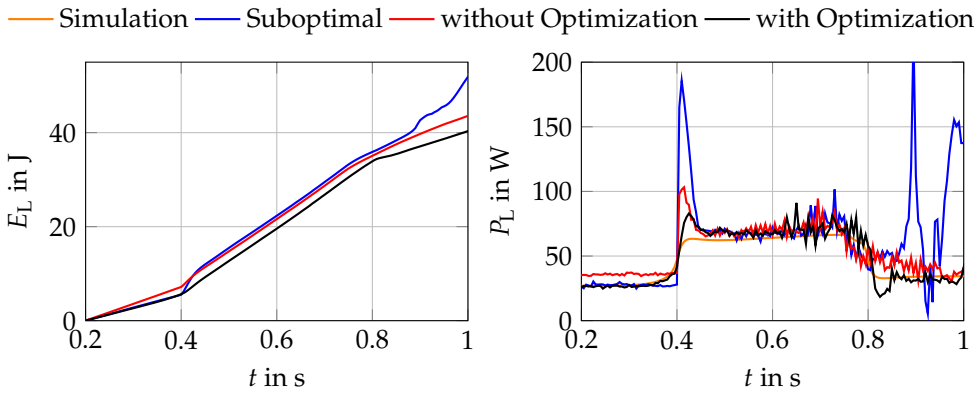

Figure 16. Comparison of measured energy and power Losses.

7.2. Template Based Solution

The idea of anticipative flux rise given in Section 3.3 was verified by a measurement. The results obtained were then compared to the results of the suboptimal procedure from [16] to illustrate the benefit of increasing the flux prior to the torque. Again, the motor described by Table A1 was used. The template was generated offline using the procedure presented in Section 4.1 and stored in a lookup table.

Figure 17 illustrates the optimal flux trajectory corresponding to the speed ramp. It can be observed that in the anticipative method, the flux rises prior to the ramp start time of $t_1 = 0.54\,\mathrm{s}$. The anticipative flux rise interval $t \in [0.4\,\mathrm{s} \quad 0.54\,\mathrm{s}]$ is 2.5 times the rotor time

constant t_R. The flux trajectory corresponding to the method specified in [16] rises at the ramp start time, as illustrated in Figure 17. Thus, the flux at the moment of the torque step will be lower, requiring a higher q-current. For the anticipative method, higher flux at the beginning of the ramp results in a lower q-current demand for the commanded torque.

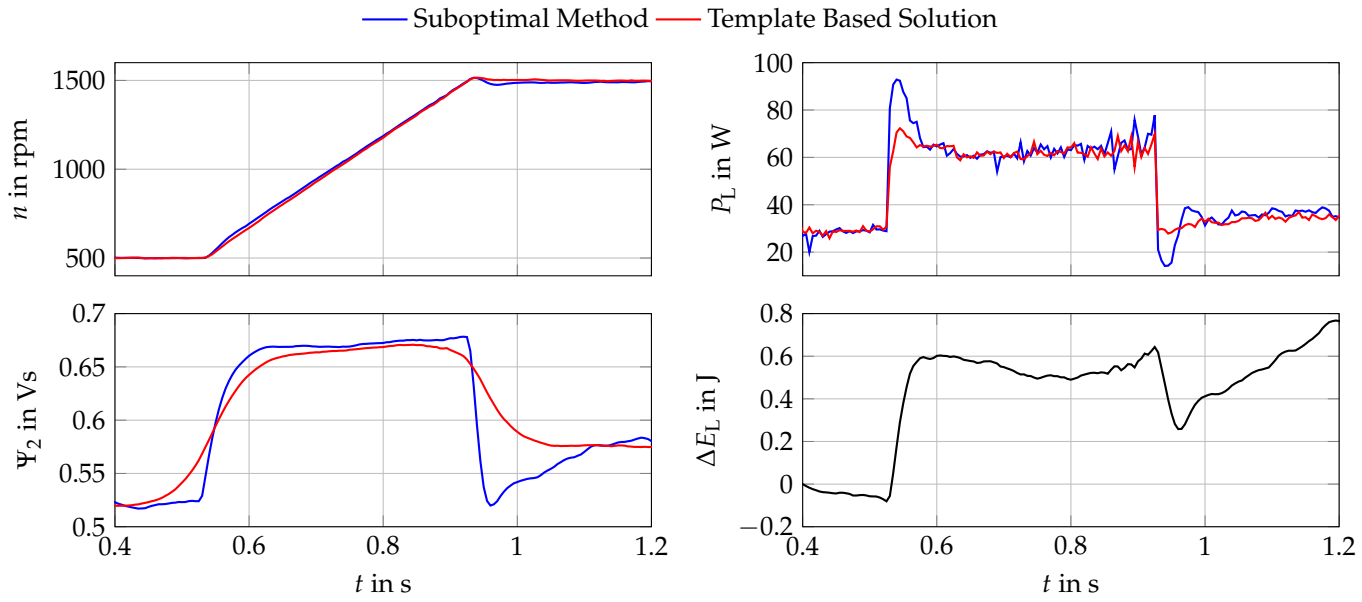

Figure 17. Measurement results for anticipative flux increase.

Figure 17 illustrates the power loss comparison using the anticipative method and the method from [16]. It can be observed that the losses during interval $t \in [0.54\,\text{s} \quad 0.6\,\text{s}]$ are less for the anticipative method compared to the suboptimal method of [16]. The saved energy $\Delta E_L = E_2 - E_1$, where E_2 is the loss energy obtained with the method of [16] and E_1 is the loss energy obtained with the anticipative flux rise method given in Figure 17. Although at the beginning, the energy losses of the new approach are higher due to the anticipative flux increase, the overall losses are lower compared to the method of [16]. This result illustrates the benefit of increasing the flux prior to the torque step.

7.3. Model Predictive Solution

The model predictive solution briefly introduced in Section 5 is now used for a comparison with a `fmincon` based solution without anticipation, in order to compare these two optimization approaches. Again, the motor from Table A1 was used. A sampling time of $\Delta t = 250\,\mu\text{s}$ was used as a compromise for the following two reasons: A lower sampling time was not possible because the GRAMPC optimizer became unstable in this setup. A higher sampling time was not possible either because then, the optimal trajectory given by GRAMPC deviated more from the steady state optimum. At $t = 0.2\,\text{s}$, a speed ramp command from 500 rpm to 1500 rpm in 0.4 s was given. In Figure 18, it can be observed that the steady state optimal flux calculated by GRAMPC is closer to that of the offline calculated trajectories. The values come closer on increasing the weightage factor of power loss in the objective functional. The ramp starts at $t = 0.2\,\text{s}$, but GRAMPC shows a tendency to first start increasing the flux and then the speed. This validates the observations made in Section 3.3, that the increase in flux prior to the torque step helps in reducing the losses in transient states.

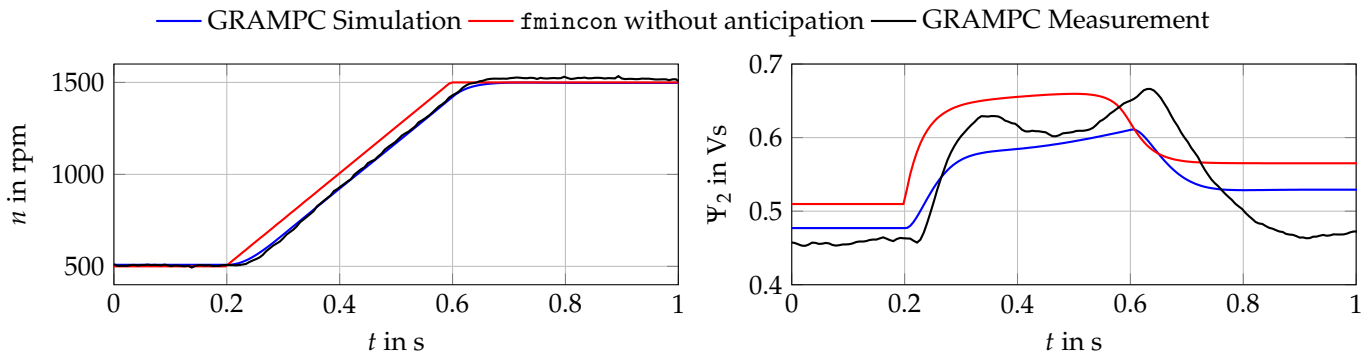

Figure 18. Measurements comparing `fmincon` based solution without anticipation to model predictive solution.

8. Application of the Template Based Solution to the WLTP Driving Cycle

To demonstrate the benefits of the methods discussed in this paper, the template adaptation algorithm was tested using the WLTP Class 3 driving cycle for light weight vehicles [30]. Using this cycle, a standardized comparison basis can be established, which models a real-world scenario. The cycle defines a speed trajectory with a sample time of 1 s. The values in between are generated by linear interpolation. This speed trajectory was used as a reference signal for the simulation. As illustrated in Section 4.2, the template adaptation algorithm is based on speed profiles. Thus, it can be directly applied to the speed profiles given by the WLTP cycle.

The simulation used the motor given in Table A1. In order to use most of the nominal speed range of the motor, the speed trajectory was multiplied by a factor of 11 rpm/kph, thus simulating a transmission and wheels. A total inertia of $J_T = 0.3405\,\mathrm{kgm}^2$ was assumed to require most of the nominal torque range of the motor. A 370 W motor was not ideal to represent an electric vehicle operation, which typically requires multiple 10 kW of rated power. This motor was chosen for consistency with respect to the other simulations and measurements presented in this paper and because it is currently the only available test bench. The power losses were integrated over the duration of the driving cycle and compared to a simulation model with no anticipation like [16], which only adjusted the optimal steady state flux according to the speed controller output.

Figure 19 shows the saved energy, when comparing the template adaptation algorithm to the optimal steady state flux control [16] over time. It is clearly visible that this approach will result in lower energy consumption and thus higher energy efficiency. Depending on the transient slope, there is more energy saved for large changes in flux and less energy saved for little changes in flux. During the periods of standstill, there is neither energy saved nor lost, which proves that for non-transient states, the steady state optimal flux is applied. The template adaptation algorithm is able to save 0.252% of the energy used by the optimal steady state flux control and 65% when compared to constant rated flux operation.

It must be considered that the WLTP driving cycle has a relatively low dynamic characteristic compared to the capabilities of electric motors. Ramps and speeds often remain nearly constant for multiple seconds, and there are many segments of standstill. The efficiency improvement will be higher with more dynamic applications.

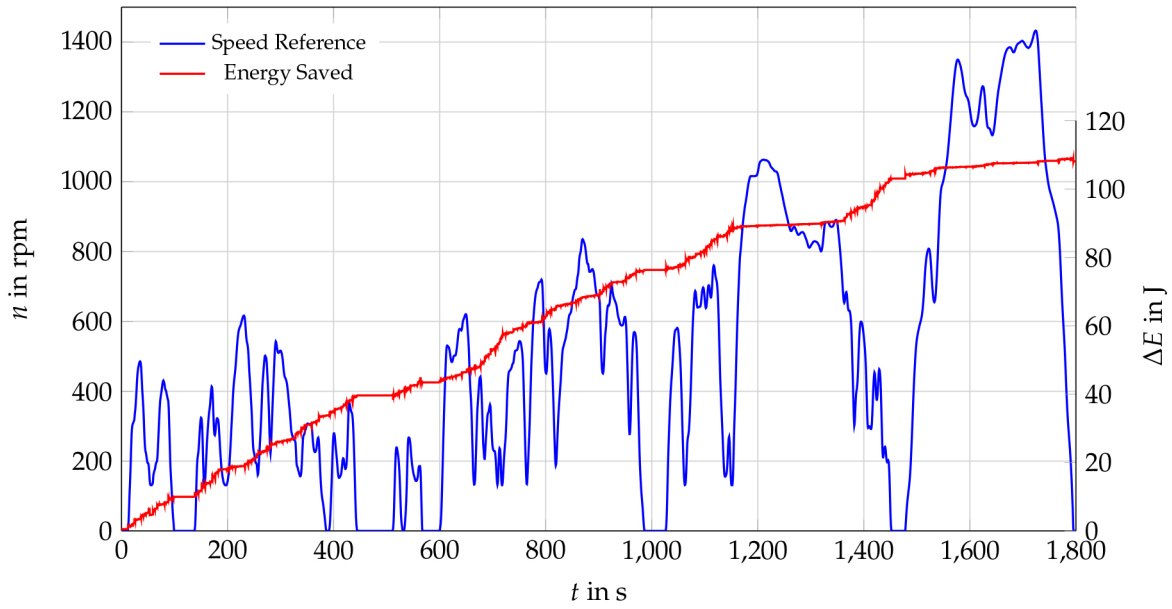

Figure 19. Simulation of saved energy using the template adaptation algorithm with the WLTP cycle.

9. Conclusions

The objective of this paper was to increase the energy efficiency of induction machines in dynamic operation. The optimization procedure considers the system dynamics given by the state equations of an induction machine, the main induction saturation effect, as well as the voltage and current limits. The procedure minimizes the losses given by a power loss model, as well as the speed error. The optimization results show that in order to decrease the losses, an anticipative flux increase to the torque step is beneficial.

To reduce the computation effort, a template is derived that resembles the shape of this anticipatory flux trajectory. This step is necessary, because the optimization procedure is a very time-consuming numerical optimization. A template can be stored in a lookup table and only needs to be adapted to fit the current driving situation, which can be done online with little computation effort. The template based solution was further enhanced by developing a template adaptation method. Using this method, any given speed trajectory and not just speed ramps can be processed. The speed trajectory was delayed by the amount of the anticipation time, to give time to modify the flux prior to the torque trajectory in order to obtain an improved energy efficiency. Although this delay may not be acceptable in every application, it will be feasible in many industrial and electric mobility applications, e.g., in manufacturing processes, where torque and speed values can be predicted to some extent, or in electric vehicles, where a small acceleration delay is already common for turbocharged combustion engines and will most likely also be accepted in order to increase the driving range. For an application in autonomous driving vehicles, the load and speed profile also will be typically known in advance due to the path planning algorithms. For periods of steady state operation, the optimal steady state flux is automatically applied by the template generation.

The template generation and anticipation time were verified by a simulation study. Measurement results proved the increased energy efficiency, when using the offline optimization procedure, as well as the template based solution. A comparison to a model predictive numerical online solution was given, which also leads to the conclusion that the modification of the flux trajectory in an anticipative manner is beneficial to minimizing the power losses in transient states, thus improving the energy efficiency of the system. Finally, the benefit of the template based solution was illustrated by applying the template and the template adaptation method to the WLTP driving cycle to prove its superiority against less optimized systems in a standardized and comparable real-world scenario.

The developed optimization methods can be further improved by taking into account the iron losses in the machine model and optimization procedure. Further testing and measurements, especially on larger machines, are necessary to refine the details of the template based solution's implementation. Finally, this solution has to be implemented in a real-world industrial or electric vehicle application.

Author Contributions: Conceptualization, G.S.; methodology, A.D. and M.W.; software, A.D. and M.W.; validation, A.D. and M.W.; investigation, A.D.; writing—original draft preparation, M.W.; writing—review and editing, G.S. and M.W.; visualization, A.D. and M.W.; supervision, G.S.; project administration, G.S.; funding acquisition, G.S. All authors have read and agreed to the published version of the manuscript.

Funding: This project "EffiDynA" was funded by the operational program Innovation and Energy Revolution. Funded by the European Union, the European Fund for regional development, and the federal state of Baden-Württemberg, Germany.

Conflicts of Interest: The authors declare no conflict of interest. The funders had no role in the design of the study; in the collection, analyses, or interpretation of data; in the writing of the manuscript; nor in the decision to publish the results.

Nomenclature

Symbol	Unit	Description
$a_0 \dots a_5$	1	Coefficients of main inductance polynomial
ΔE_L	J	Difference in energy lost
E_1	J	Energy lost of new approach
E_2	J	Energy lost of reference approaches
$\underline{I}_1$	A	Stator current phasor
I_1d	A	Stator d-current component
$I_\mathrm{1d,opt,\infty}$	A	Stator optimal d-current component in static operation
$I_\mathrm{1d,ref}$	A	Reference stator d-current for the current controller
$I_\mathrm{1d,act}$	A	Actual stator d-current for the current controller
I_1q	A	Stator q-current component
$I_\mathrm{1,max}$	A	Maximum stator current phasor length
$\underline{I}_2$	A	Rotor current phasor
$\underline{I}_{L_\mu}$	A	Current phasor through main inductance
$\underline{I}_{R_\mathrm{Fe}}$	A	Current phasor through iron resistance
J	1	Objective functional
J_d	1	Discretized objective functional
q	$\mathrm{W}/(\mathrm{rad\,s^{-1}})^2$	Weightage factor for specifying optimization priorities
J_M	$\mathrm{kgm^2}$	Moment of inertia of the motor
J_L	$\mathrm{kgm^2}$	Moment of inertia of the load
J_T	$\mathrm{kgm^2}$	Total moment of inertia of the entire drive train
k	1	Sample number counter
N	1	Total number of samples
L_σ	H	Stray inductance
L_μ	H	Main inductance
ω_1	rad/s	Stator angular frequency
ω_2	rad/s	Slip angular frequency
ω_Rm	rad/s	Rotor mechanical angular frequency
$\omega_\mathrm{Rm,ref}$	rad/s	Rotor mechanical angular frequency reference for the speed controller
$\omega_\mathrm{Rm,act}$	rad/s	Actual rotor mechanical angular frequency for the current controller
P_L	W	Power loss
Ψ_1d	Vs	Stator flux linkage d-component
Ψ_1q	Vs	Stator flux linkage q-component
$\underline{\Psi}_2$	Vs	Rotor flux linkage phasor
Ψ_2d	Vs	Rotor flux linkage d-component
Ψ_2q	Vs	Rotor flux linkage q-component

Symbol	Unit	Description
$\Psi_{2,\mathrm{opt}}$	Vs	Optimal rotor flux linkage
$\Psi_{2,\mathrm{opt},\infty}$	Vs	Optimal rotor flux linkage in static operation
$\Psi_{2,\mathrm{template}}$	Vs	Rotor flux linkage according to the template
$\Psi_{2,\mathrm{ref}}$	Vs	Rotor flux linkage reference for the flux controller
$\Psi_{2,\mathrm{act}}$	Vs	Actual rotor flux linkage for the flux controller
R_1	Ω	Stator copper resistance
R_2	Ω	Rotor copper resistance
R_{Fe}	Ω	Iron resistance
t	s	Time
t_0	s	Start time of the optimization interval
Δt_a	s	Anticipative time
t_f	s	End time of the optimization interval
t_R	s	Rotor time constant
t_s	s	Sample time
T_L	Nm	Load torque
T_Mi	Nm	Torque produced by the motor
T_ref	Nm	Reference torque
$\underline{U}_1$	V	Stator voltage phasor
$U_{1,\mathrm{max}}$	V	Maximum length of stator voltage phasor
$U_{1\mathrm{d}}$	V	Stator voltage d-component
$U_{1\mathrm{q}}$	V	Stator voltage q-component
Z_p	-	Number of pole pairs

Abbreviations

The following abbreviations are used in this manuscript:

fmincon	MATLAB find minimum of constrained nonlinear multivariable function
GRAMPC	A gradient-based augmented Lagrangian framework for embedded NMPC
WLTP	World Harmonised Light Weight Vehicles Test Procedure

Appendix A. Motor Parameters

Table A1. Motor data of the 370 W induction machine.

P_N	370 W	T_N	2.59 Nm
Z_p	2	J_M	$22 \cdot 10^{-4}\,\mathrm{kg\,m^2}$
n_N	1370 rpm		
R_1	27.8 Ω	R_2	17.24 Ω
R_{Fe}	2300 Ω		
L_μ	0.6 H	L_σ	0.142 H
t_R	35 ms		
a_1	−0.669	a_2	3.606
a_3	−6.622	a_4	4.415
a_5	−0.743	a_6	0.754
t_1	0.42 s	t_2	0.56 s
t_3	0.62 s	t_4	0.76 s
t_5	0.9 s		
C_1	0.0013	C_2	0.5778
$\omega_{\mathrm{Rm},1}$	52.36 rad/s≙500 rpm	$\omega_{\mathrm{Rm},2}$	188.49 rad/s≙1800 rpm
T_L	0.645 Nm		

References

1. Bailey, G.; Mancheri, N.; van Acker, K. Sustainability of Permanent Rare Earth Magnet Motors in (H)EV Industry. *J. Sustain. Metall.* **2017**, *3*, 611–626. [CrossRef]
2. Rassolkin, A.; Heidari, H.; Kallaste, A.; Vaimann, T.; Acedo, J.P.; Romero-Cadaval, E. Efficiency Map Comparison of Induction and Synchronous Reluctance Motors. In Proceedings of the 2019 26th International Workshop on Electric Drives: Improvement in Efficiency of Electric Drives (IWED), Moscow, Russia, 30 January–2 February 2019; pp. 1–4. [CrossRef]
3. Kim, S.; Sul, S.K.; Ide, K.; Morimoto, S. Maximum efficiency operation of Synchronous Reluctance Machine using signal injection. In Proceedings of the 2010 International Power Electronics Conference—ECCE ASIA, Sapporo, Japan, 21–24 June 2010; pp. 2000–2004. [CrossRef]

4. Bazzi, A.M.; Krein, P.T. Review of Methods for Real-Time Loss Minimization in Induction Machines. *IEEE Trans. Ind. Appl.* **2010**, *46*, 2319–2328. [CrossRef]
5. Kioskeridis, I.; Margaris, N. Loss Minimization in Scalar—Controlled Induction Motor Drives with Search Controllers. *IEEE Trans. Power Electron.* **1996**, *11*, 213–220. [CrossRef]
6. Consoli, A.; Scarcella, G.; Scelba, G.; Cacciato, M. Energy Efficient Sensorless Scalar Control for Full Speed Operating Range IM Drives. In Proceedings of the 14th European Conference on Power Electronics and Applications, Birmingham, UK, 30 August–1 September 2011; pp. 1–10.
7. Uddin, M.N.; Nam, S.W. New Online Loss—Minimization–Based Control of an Induction Motor Drive. *IEEE Trans. Power Electron.* **2008**, *23*, 926–933. [CrossRef]
8. Qu, Z.; Ranta, M.; Hinkkanen, M.; Luomi, J. Loss-Minimizing Flux Level Control of Induction Motor Drives. *IEEE Trans. Ind. Appl.* **2012**, *48*, 952–961. [CrossRef]
9. Windisch, T.; Hofmann, W. A Novel Approach to MTPA Tracking Control of AC Drives in Vehicle Propulsion Systems. *IEEE Trans. Veh. Technol.* **2018**, *67*, 9294–9302. [CrossRef]
10. Chakraborty, C.; Hori, Y. Fast Efficiency Optimization Techniques for the Indirect Vector–Controlled Induction Motor Drives. *IEEE Trans. Ind. Appl.* **2003**, *39*, 1070–1076. [CrossRef]
11. Wang, Y.; Ito, T.; Lorenz, R.D. Loss Manipulation Capabilities of Deadbeat–Direct Torque and Flux Control Induction Machine Drives. *IEEE Trans. Ind. Appl.* **2015**, *51*, 4554–4566. [CrossRef]
12. Lorenz, R.D.; Yang, S.M. Efficiency–Optimized Flux Trajectories for Closed–Cycle Operation of Field-Orientation Induction Machine Drives. *IEEE Trans. Ind. Appl.* **1992**, *28*, 574–580. [CrossRef]
13. Lorenz, R.D.; Yang, S.M. AC Induction Servo Sizing for Motion Control Applications via Loss Minimizing Real–Time Flux Control. *IEEE Trans. Ind. Appl.* **1992**, *28*, 589–593. [CrossRef]
14. Klenke, F.; Hofmann, W. Energy-Efficient Control of Induction Motor Servo Drives With Optimized Motion and Flux Trajectories. In Proceedings of the 14th European Conference on Power Electronics and Applications, Birmingham, UK, 30 August–1 September 2011; pp. 1–7.
15. Stumper, J.F.; Dötlinger, A.; Kennel, R. Loss Minimization of Induction Machines in Dynamic Operation. *IEEE Trans. Energy Convers.* **2013**, *28*, 726–735. [CrossRef]
16. Borisevich, A.; Schullerus, G. Energy Efficient Control of an Induction Machine Under Torque Step Changes. *IEEE Trans. Energy Convers.* **2016**, *31*, 1295–1303. [CrossRef]
17. Grčar, B.; Hofer, A.; Štumberger, G. Induction Machine Control for a Wide Range of Drive Requirements. *Energies* **2020**, *13*, 175. [CrossRef]
18. Diachenko, G.; Schullerus, G. Simple Dynamic Energy Efficient Field Oriented Control in Induction Motors. In Proceedings of the 18th International Symposium Power Electronics Ee2015, Belgrade, Serbia, 22–24 April 2015; pp. 1–5.
19. Weis, R.; Gensior, A. A Model-Based Loss-Reduction Scheme for Transient Operation of Induction Machines. *EPE* **2016**, *2016*, 1–8. [CrossRef]
20. Plathottam, S.J.; Salehfar, H. Transient Energy Efficiency Analysis of Field Oriented Induction Machines. *IEEE Access* **2017**, *5*, 20545–20556. [CrossRef]
21. Abdelati, R.; Mimouni, M.F. Optimal control strategy of an induction motor for loss minimization using Pontryaguin principle. *Eur. J. Control* **2019**, *49*, 94–106. [CrossRef]
22. Diachenko, G.G.; Schullerus, G.; Dominic, A.; Aziukovskyi, O.O. Energy-efficient predictive control for field-orientation induction machine drives. *Nauk. Visnyk Natsionalnoho Hirnychoho Universytetu* **2020**, 61–67. [CrossRef]
23. Hu, Z.; Liu, Q.; Hameyer, K. Loss Minimization of Speed Controlled Induction Machines in Transient States Considering System Constraints. In Proceedings of the 2014 17th International Conference on Electrical Machines and Systems (ICEMS), Hangzhou, China, 22–25 October 2014; pp. 123–129. [CrossRef]
24. Dominic, A.; Schullerus, G.; Winter, M. Optimal Flux and Current Trajectories for Efficient Operation of Induction Machines. In Proceedings of the 2019 20th International Symposium on Power Electronics (Ee), Novi Sad, Serbia, 23–26 October 2019; pp. 1–6. [CrossRef]
25. Dominic, A.; Schullerus, G.; Winter, M. Anticipative Flux Trajectories for Dynamic Energy Efficient Operation of Induction Machines. In Proceedings of the 2020 IEEE Transportation Electrification Conference & Expo (ITEC), Chicago, IL, USA, 24–26 June 2020; pp. 1038–1043. [CrossRef]
26. Dominic, A.; Schullerus, G.; Winter, M. Rotor Flux Templates for Energy Efficient Dynamic Operation of Induction Machines. In Proceedings of the 2020 International Conference on Electrical Machines (ICEM), Gothenburg, Sweden, 23–26 August 2020; pp. 312–318. [CrossRef]
27. Englert, T.; Völz, A.; Mesmer, F.; Rhein, S.; Graichen, K. A software framework for embedded nonlinear model predictive control using a gradient-based augmented Lagrangian approach (GRAMPC). *Optim. Eng.* **2019**, *20*, 769–809. [CrossRef]
28. Quang, N.P.; Dittrich, J.A. *Vector Control of Three-Phase AC Machines: System Development in the Practice*; Power Systems; Springer: Berlin/Heidelberg, Germany, 2008.

29. Pucci, M. State-Space Space-Vector Model of the Induction Motor Including Magnetic Saturation and Iron Losses. *IEEE Trans. Ind. Appl.* **2019**, *55*, 3453–3468. [CrossRef]
30. United Nations. *Global Registry, Created on 18 November 2004, Pursuant to Article 6 of the Agreement Concerning the Establishing of Global Technical Regulations for Wheeled Vehicles, Equipment and Parts Which Can Be Fitted and/or Be Used on Wheeled Vehicles (ECE/TRANS/132 and Corr.1) Done at Geneva on 25 June 1998: Addendum 15: Global Technical Regulation No. 15, Worldwide Harmonized Light Vehicles Test Procedure: Established in the Global Registry on 12 March 2014*; United Nations: New York, NY, USA, 2014.